

AN ANALYTICAL INVESTIGATION ON THE FRACTURE BEHAVIOUR OF COMPACT-TENSION TEST SPECIMENS

Ignacio Villa^a and José Fernández-Sáez^b

^a*Departamento de Construcciones, Facultad de Ingeniería, Universidad Nacional de La Plata.
Calle 48 y 115 s/n, (B1900TAG) La Plata, Buenos Aires, República Argentina.
eivilla@ing.unlp.edu.ar, <http://www.ing.unlp.edu.ar/departamentos/construcciones/>*

^b*Departamento de Mecánica de Medios Continuos y Teoría de Estructuras,
Universidad Carlos III de Madrid. Av. de la Universidad, 30. 28911 Leganés, Madrid, España.
ppfer@ing.uc3m.es, http://www.uc3m.es/portal/page/portal/dpto_mec_med_cont_teor_est*

Keywords: Cohesive-crack model, weight-function technique, fracture behaviour, compact-tension test specimen.

Abstract. An analytical investigation on the fracture behaviour of a typical compact-tension (*CT*) test specimen is presented within the framework of the well-known weight-function technique. Simulations of this test configuration, extensively used for determining the fracture properties of a wide range of materials, have been carried out. The influence of the initial crack length is considered and a cohesive-crack model is used to establish the relevant displacement fields as well as the *load – displacement* curve. Plane-strain finite-element models were built and comparisons with these results show that the weight-function method yields results without any appreciable error. In addition, observations of fracture behaviour in a *CT* specimen of Polymethyl methacrylate (*PMMA*) are used to assess the relevance of the theoretical results as well. Excellent agreement has also been achieved when comparing these experimental results available in the literature with the theoretical predictions.

1 INTRODUCTION

In recent decades, requirements for high loading capacity, weight reduction, and low production cost of engineering structures, combined with high structural safety, have to be met by new design concepts. Special efforts have been made to guarantee the structural integrity of mechanical components, especially when the presence of defects is considered. The latter may appear as a result of manufacturing processes, transportation or assembly of components, although defects generally arise throughout the structure's service life.

When safety has to be ensured, expensive test programs should be applied. Accurate models based on fracture mechanics could help to reduce laboratory testing. Indeed, once created the mathematical model, it is relatively easy to change the model parameters such as geometry, boundary conditions and material properties to study its incidence on the fracture behaviour.

One of the most widely used theories for this purpose is Linear Elastic Fracture Mechanics (*LEFM*). In this theory, applicable only when the stress concentrators are cracks, the main hypothesis is the existence of a nonlinear zone ahead of the crack tip of negligible size. As soon as the notch is blunted the stress singularity disappears and *LEFM* is no longer applicable.

Besides the classical nonlinear fracture approach, cohesive-crack models (*CCM*) are being increasingly used to describe the fracture behaviour of a wide range of materials, including ceramics, polymers, ductile metals, and composites, when the size of the nonlinear zone ahead of the crack tip may be important compared to all other relevant dimensions of the problem, preventing the use of *LEFM*.

Its basic ideas were originally formulated by Dugdale ([Dugdale, 1960](#)), assuming that the stress on the crack line ahead of the crack tip was limited by the yield stress. The plastic deformation was concentrated along the crack line, generating a displacement discontinuity similar to a crack. Dugdale's model did not include any softening or fracture criterion. It was a purely plastic model also known as the strip yield model.

Barenblatt ([Barenblatt, 1962](#)) proposed a simple model to represent the nonlinear behaviour ahead of the tip of a preexisting crack. He showed that the cohesive zone made it possible to relieve the crack tip singularity while for large cracks the *LEFM* equations were preserved. The fracture energy G_F was related to the interatomic potential. His analysis was limited to very large cracks compared to the cohesive zone itself.

In the late seventies, Hillerborg et al. ([Hillerborg et al., 1976](#)) postulated the fictitious crack model by proposing that a cohesive crack may be assumed to develop anywhere, even if no preexisting macrocrack is actually present. It is easily to show that when the fictitious crack model is used to describe the behaviour of a preexisting crack, the mathematical formalism is identical to that for the *CCM*.

This approach has been used to model the crack growth in concrete ([Reinhardt, 1984](#)), ([Hillerborg, 1985](#)), ceramics ([Foote et al., 1986](#)), ([Mai and Lawn, 1987](#)), polymers ([Knauss, 1973](#)), ([Williams, 1984](#)), ([Tijssens et al., 2000](#)) and metals ([Tvergaard and Hutchinson, 1992](#)), ([Yuan et al., 1996](#)). Since *CCM* were proposed for the first time, different methods have been developed to solve a problem within this framework. Considering the zone surrounding the cohesive crack as linear elastic, Ungsuwarungsri and Knauss ([Ungsuwarungsri and Knauss, 1988a](#)), ([Ungsuwarungsri and Knauss, 1988b](#)), Knauss ([Knauss, 1993](#)) and Bažant and Planas ([Bažant and Planas, 1998](#)) used the Green's function approach. Other available methods are the Petersson influence method ([Petersson, 1981](#)) and the superposed-cracks method, proposed by Planas and Elices ([Planas and Elices, 1986](#)), ([Planas and Elices, 1992](#)) and modified by Bažant ([Bažant, 1990](#)) and Bažant and Beissel ([Bažant and Beissel, 1994](#)).

One of the major limitations of this approach is the need to assess numerically the Green function for selected cases, implying an important limitation in practice. Moreover, these procedures require prior numerical results, thus limiting their use when the geometry or the size of the solid must be changed.

In the present work, an analytical investigation on the fracture behaviour of compact-tension (*CT*) test specimens is summarized by applying the weight-function technique. Simulations of this test configuration, extensively used to determine the fracture properties of a wide range of materials, have been performed. The influence of the initial crack length is considered and a cohesive-crack model is used to establish the relevant displacement fields as well as the *load – CMOD* response.

In addition to the material properties and the weight function, only a general expression of the Stress Intensity Factor (*SIF*) for the cracked geometry is needed to use the proposed method. This procedure can be easily implemented to solve a problem with any geometry and does not require previous numerical results. It has important advantages in comparison to other available methods such as better ability to modify the geometry or the size of the test specimens as well as the softening curve of the material.

This paper begins by introducing a general outline of the cohesive-crack model. In Section 3 the weight-function technique is developed and a description of the problem to be solved and the results of the analytical modeling are shown in Section 4. The following section deals with the finite element modeling of a *CT* specimen and the results of its fracture behaviour are presented. The paper concludes with the validation of the analytical method with numerical as well as experimental results and final remarks.

2 OUTLINE OF THE COHESIVE-CRACK MODEL

Fracture behaviour of some materials such as concrete, ceramics, and composites (i.e. so-called quasi-brittle materials) is characterized by the location of a nonlinear zone near the crack tip. The cohesive crack model (*CCM*), which extends the ideas of Dugdale (Dugdale, 1960) and Barenblatt (Barenblatt, 1962), is now a well-established approach in computational fracture mechanics to analyse these kinds of problems.

The basic assumption is the existence of a crack (normally termed as cohesive or fictitious crack) able to transfer stress from one face to the other while opening, as shown in Fig. 1.

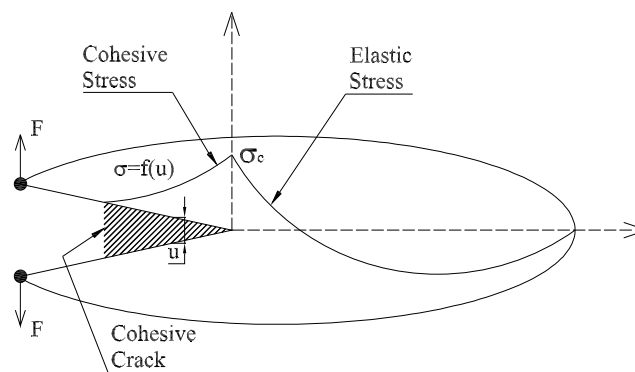


Figure 1: Two-dimensional body containing a cohesive crack

Cohesive-crack models are versatile and effective tools for numerical simulation of various separation phenomena in solids. The simplest assumptions regarding *CCM* are as follows:

- The bulk material is considered as linear-elastic with Young modulus E and Poisson ratio ν .
- As soon as the cohesive stress, σ_c , is reached at any point in the material, a cohesive crack perpendicular to the cohesive stress direction occurs.
- From then on, a crack of length a is considered, corresponding to the amount of the initial crack length, a_0 , and the process zone, Δ_a .
- The analysis is restricted to mode I . The cohesive stress transferred at any point is a unique function of the crack opening, as illustrated in Fig. 2 and is assumed to be a material property called the softening curve:

$$\sigma = f(u) \quad (1)$$

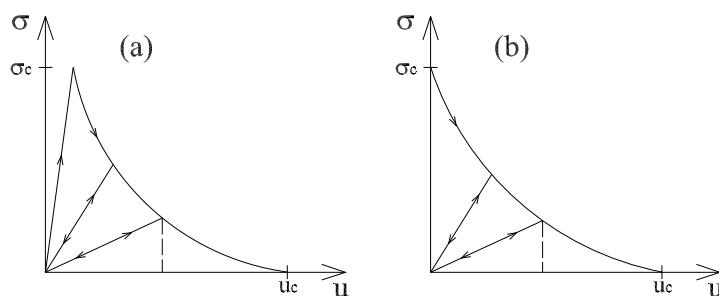


Figure 2: General definition of the softening curve: (a) initially elastic; (b) initially rigid

- The area under the softening curve is the fracture-energy release rate, G_F , and is the external energy supply required to create and fully break a unit surface area of cohesive crack.
- A further parameter related to the critical size of the process zone is the characteristic length, l_c , defined as follows:

$$l_c = E' \frac{G_F}{\sigma_c^2} \quad (2)$$

where $E' = E$ for plane stress and $E' = E/(1 - \nu^2)$ for plane strain.

There are two basic types of *CCM* which are distinguished mainly by the presence of the initial elastic curve. In the case of initially elastic cohesive laws, Fig. 2 (a), the closing traction is initially zero at zero separation. Under monotonic separation, the traction increases with growing separation until a maximum value is reached, after which the traction diminishes to zero at some finite relative displacement. The compliance introduced by these kinds of cohesive laws has no physical explanation but is generally of little consequence where only a single pre-existing surface is designated as the fracture surface. This is appropriate for symmetrical cases where the crack path can be easily inferred.

On the other hand, an initially rigid class of cohesive laws, Fig. 2 (b), down hold that the prospective separation surfaces remain connected until a critical traction is reached, whereupon the traction declines continuously to zero as separation proceeds. In both cases the post-peak unload/reload behaviour is generally assumed to occur along a straight trajectory from the origin.

Most existing analytical methods has been developed to analyse a two-dimensional cracked body in mode *I*. The problem consists of the determination of the cohesive zone length, stresses within that zone and the displacement field into a 2D cracked body under a boundary-loading system. The solution is based on the discretization of the cracked section as sketched in Fig. 3, which is easily determined from the symmetrical mode *I* loading conditions, into $M' + 1$ nodes separated by a distance $h = W/M'$ where W is a representative dimension of the geometry, defining the following three zones:

1. Initial notch: spanning the nodes 1 and N .
2. Cohesive zone: extended between the nodes $N + 1$ and C .
3. Uncracked ligament: include the node C to node $M' + 1$.

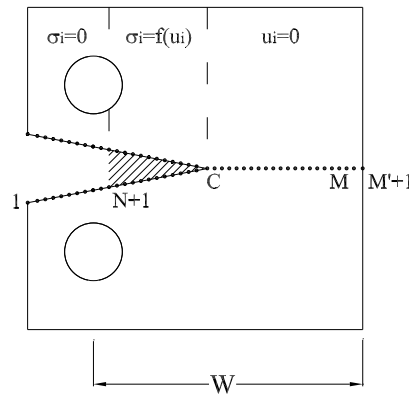


Figure 3: Node layout of the analytical methods

The following equations must be satisfied along the central cross-section:

$$\sigma_i = 0 \quad i = 1, \dots, N \quad (3)$$

$$\sigma_i = f(u_i) \quad i = N + 1, \dots, C \quad (4)$$

$$u_i = 0 \quad i = C, \dots, M \quad (5)$$

where σ_i are the nodal stresses and u_i are the nodal crack openings. Eq. (4) and Eq. (5) must to be satisfied at node C which implies that this node is the cohesive-crack tip.

3 THE WEIGHT-FUNCTION TECHNIQUE

According to its definition, the relationship between K_I and the strain energy release rate, G , can be written in terms of the crack length, a , as follows:

$$G = \frac{K_I^2}{E'} = \frac{\partial U}{\partial a} = \frac{1}{2} \int_a \sigma_i(x) \frac{\partial u(x, a)}{\partial a} dx \quad (6)$$

in which

$$U = \frac{1}{2} \int_a \sigma_i(x) u(x, a) dx \quad (7)$$

is the strain energy, $\sigma_i(x)$ is the stress distribution along the x -axis and $u(x, a)$ is the crack shape.

With the rearrangement of Eq. (6) the following expression is achieved:

$$K_I = \int_a \sigma_i(x) m(x, a) dx \quad (8)$$

where

$$m(x, a) = \frac{E'}{2K_I} \frac{\partial u(x, a)}{\partial a} \quad (9)$$

is the weight function first introduced by Bueckner (Bueckner, 1970) and Rice (Rice, 1972), who have demonstrated that $m(x, a)$ is unique to the given geometry, and is independent of the loading from which it was derived.

4 PROBLEM FORMULATION AND ITS SOLUTION

The fracture toughness of a wide range of materials is usually measured by using both the three-point bending (*TPB*) test or the double-cantilever beam (*DCB*) test. For materials delivered in the form of sheets a solution may be found by using a compact-tension (*CT*) test such as that depicted in Fig. 4. This specimen, initially developed for the study of crack propagations in metallic materials, can be used to determine the fracture toughness of composite laminates as well. In such configurations it is desirable for the fracture path to follow essentially the prolongation of the crack starter and not deviate strongly to one side.

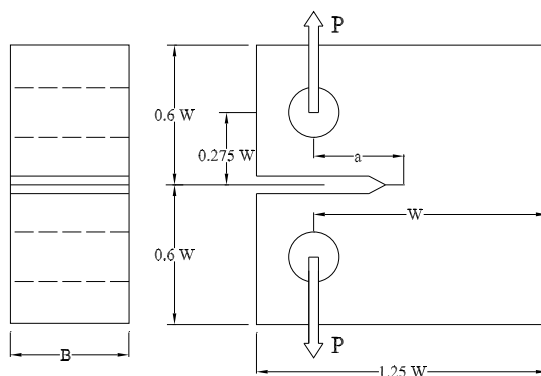


Figure 4: General layout of the compact-tension specimen

For a given value of the external load P , the problem consists on determining of the cohesive zone length, the stresses within that zone, and the associated displacements field. In addition to the weight function and a general expression for the stress-intensity factor, the data required to solve the problem is as follows:

- The dimensions of the specimen.
- The initial crack length, a_0 .

- The external load, P .
- The constitutive equation outside the cohesive zone.
- The softening curve, $\sigma = f(u)$.

A general expression to evaluate the SIF in a CT specimen proposed by Srawley and Gross (Srawley and Gross, 1972) will be used:

$$K_{I\infty} = \frac{P(2W + a)}{B(W - a)^{3/2}} f^*(\alpha) \quad (10)$$

where B is the specimen width, W is the loaded length, the load is denoted by P and α is the non-dimension crack length, given by:

$$\alpha = \frac{a}{W} \quad (11)$$

The function $f^*(\alpha)$ has been tabulated by Srawley and Gross (Srawley and Gross, 1972) using the boundary collocation method. The corresponding values are shown in Table 1.

α	$f^*(\alpha)$
0.3	1.466
0.4	1.419
0.5	1.364
0.6	1.327
0.7	1.312
0.8	1.312

Table 1: Tabulated values of $f^*(\alpha)$, Eq. (10).

Since the resolution of the proposed method requires the determination of the SIF at as many points as the discretization of the axis of crack propagation has (may be hundreds or even thousands, depending on the characteristic length of the material), the tabulated values of $f^*(\alpha)$ have been adjusted using a fourth-degree polynomial, yielding the following expression:

$$f^*(\alpha) = 1,08 + 3,97\alpha - 13,25\alpha^2 + 16,30\alpha^3 - 6,88\alpha^4 \quad (12)$$

As shown in Fig. 5, an excellent agreement is achieved between the polynomial fit and the values proposed by Srawley and Gross (Srawley and Gross, 1972).

The weight function used has been proposed by Fett and Munz (Fett and Munz, 1997):

$$m(x, a) = \sqrt{\frac{2}{\pi a}} \frac{1}{\sqrt{1-\rho}} \left\{ 1 + \sum_{\eta=1}^4 \sum_{\mu=1}^5 \frac{A_{\eta\mu} \alpha^{\mu-1}}{(1-\alpha)^{3/2}} (1-\rho)^\eta \right\} \quad (13)$$

where

$$\alpha = \frac{a}{W} \quad ; \quad \rho = \frac{x}{a} \quad (14)$$

and the constants $A_{\eta\mu}$ are shown in Table 2 below.

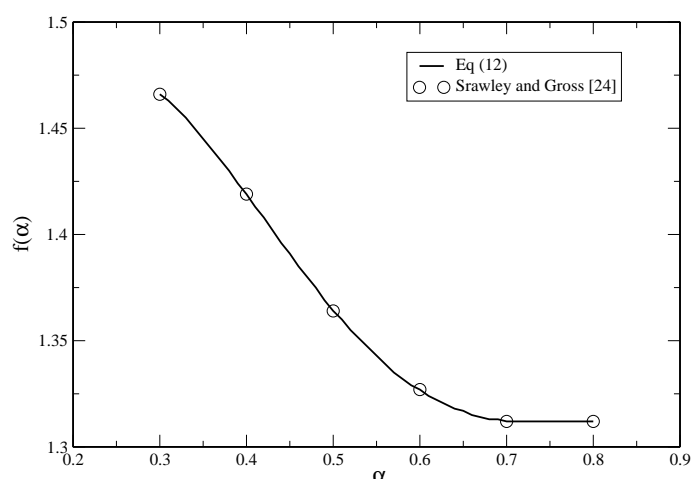


Figure 5: Polynomial fit of the values proposed by Srawley and Gross (Srawley and Gross, 1972)

η	$\mu=1$	2	3	4	5
1	2.673	-8.604	20.621	-14.635	0.477
2	-3.557	24.9726	-53.398	50.707	-11.837
3	1.230	-8.411	16.957	-12.157	-0.940
4	-0.157	0.954	-1.284	-0.393	1.655

Table 2: Coefficients of the weight function, Eq. (13).

The displacement field generated by the external load, $u_\infty(x, a)$, could be determined by integrating Eq. (9). Setting the weight function in dimensionless form, i.e.:

$$m(x, a) = \frac{1}{\sqrt{W}} \bar{m}(\bar{x}_i, \alpha) \quad (15)$$

where

$$\bar{m}(\bar{x}_i, \alpha) = \sqrt{\frac{2}{\pi}} \frac{1}{\sqrt{\alpha - \bar{x}_i}} \left\{ 1 + \frac{(1 - \rho_i)}{(1 - \alpha)^{3/2}} \tilde{H}(\alpha) \right\} \quad (16)$$

the following expression is found to define the displacement field due to the external load:

$$u_\infty(\bar{x}_i, \alpha_i) = \frac{\sqrt{W}}{E'} \int_{\bar{x}_i}^{\alpha_i} K_{I\infty} \bar{m}(\bar{x}_i, \alpha) d\alpha \quad (17)$$

in which

$$\bar{x}_i = \frac{x_i}{W} \quad (18)$$

and $\tilde{H}(\alpha)$ can be found in the appendix.

From Eq. (10), (16) and (17) the following expression for the displacements caused by the external load is formulated:

$$u_\infty(\bar{x}_i, \alpha_i) = \frac{P}{E'b} \sqrt{\frac{2}{\pi}} \int_{\bar{x}_i}^{\alpha_i} \frac{f^*(\alpha)(2 + \alpha)}{(1 - \alpha)^{3/2}(\alpha - \bar{x}_i)^{1/2}} \left(1 + \frac{(1 - \rho_i)}{(1 - \alpha)^{3/2}} \tilde{H}(\alpha) \right) d\alpha \quad (19)$$

The integral in Eq. (19) is not defined in the lower limit of integration, and thus, when the following change of variable is made:

$$\alpha = \bar{x}_i + t^2 = \Delta_t \quad (20)$$

the following expression results, which can be solved numerically:

$$u_{\infty}(\bar{x}_i, \alpha_i) = \frac{2P}{E'b} \sqrt{\frac{2}{\pi}} \int_0^{\sqrt{\alpha_i - \bar{x}_i}} \frac{f^*(\Delta_t)(2 + \Delta_t)}{(1 - \Delta_t)^{3/2}} \left(1 + \frac{t^2}{\Delta_t(1 - \Delta_t)^{3/2}} \widetilde{H}_1(t) \right) dt \quad (21)$$

where the function $f^*(\Delta_t)$ is given by:

$$f^*(\Delta_t) = 1,08 + 3,97\Delta_t - 13,25\Delta_t^2 + 16,30\Delta_t^3 - 6,88\Delta_t^4 \quad (22)$$

and analytical expression of $\widetilde{H}_1(t)$ can be found in the appendix.

In the present work a linear softening curve is considered, i.e.:

$$\sigma_i(\bar{x}) = \tau + \zeta u(\bar{x}, \alpha) \quad (23)$$

in which the parameters τ and ζ take the following values:

$$\begin{aligned} \tau = \sigma_c & \quad ; & \quad \zeta = -\sigma_c/u_c & \quad \text{if } u < u_c \\ \tau = 0 & \quad ; & \quad \zeta = 0 & \quad \text{if } u \geq u_c \end{aligned} \quad (24)$$

Taken into account that cohesive stress is different from zero only in the cohesive zone, i.e.:

$$\sigma_i(\bar{x}) = \begin{cases} \sigma_i(\bar{x}) & \text{if } \alpha_0 \leq \bar{x} \leq \alpha \\ 0 & \text{if } \bar{x} < \alpha_0 \end{cases} \quad (25)$$

and replacing Eq. (15) into Eq. (8), it is possible to get the *SIF* due to the cohesive stress as:

$$K_{Icohe} = \sqrt{\frac{2W}{\pi}} \int_{\alpha_0}^{\alpha_i} \frac{\sigma_i(\bar{x}, \alpha_i)}{\sqrt{\alpha_i - \bar{x}}} \left\{ 1 + \frac{(1 - \bar{\rho})}{(1 - \alpha_i)^{3/2}} H(\bar{x}) \right\} d\bar{x} \quad (26)$$

where

$$\bar{\rho} = \frac{\bar{x}}{\alpha_i} \quad (27)$$

and $H(\bar{x})$ can be found in the appendix.

As can be seen, the integral in Eq. (26) is not defined in the upper limit of integration. Therefore, it is necessary to make a change of variable, which in this case is given by:

$$\bar{x} = \alpha_i - t^2 \quad (28)$$

After some algebra, the following expression for K_{Icohe} is found:

$$K_{Icohe} = 2\sqrt{\frac{2W}{\pi}} \int_0^{\sqrt{\alpha_i - \alpha_0}} \sigma_i(\alpha_i, t) \left\{ 1 + \frac{t^2}{\alpha_i(1 - \alpha_i)^{3/2}} H_2(t) \right\} dt \quad (29)$$

where the function $H_2(t)$ is reported in the appendix.

Integrating Eq. (9) the displacement field caused by the cohesive stress is determined:

$$u_{cohe}(\bar{x}_i, \alpha_i) = \frac{\sqrt{W}}{E'} \int_{\bar{x}_i}^{\alpha_i} K_{Icohe} \bar{m}(\bar{x}_i, \alpha) d\alpha \quad (30)$$

in which $\bar{m}(\bar{x}_i, \alpha)$ is the weight function in dimensionless form. Thus, Eq. (30) may be rewritten in the following way:

$$u_{cohe}(\bar{x}_i, \alpha_i) = \frac{1}{E'} \sqrt{\frac{2W}{\pi}} \int_{\bar{x}_i}^{\alpha_i} \frac{K_{Icohe}}{\sqrt{\alpha - \bar{x}_i}} \left(1 + \frac{(1 - \rho_i)}{(1 - \alpha)^{3/2}} H(\alpha) \right) d\alpha \quad (31)$$

Since the last integral is not defined in the lower limit of integration, it is necessary to make the change of variable that is shown in Eq. (20) again, giving the following expression, which makes it possible to calculate the crack profile caused by the cohesive stress:

$$u_{cohe}(\bar{x}_i, \alpha_i) = \frac{1}{E'} \sqrt{\frac{8W}{\pi}} \int_0^{\sqrt{\alpha_i - \bar{x}_i}} K_{Icohe}(t) \left(1 + \frac{t^2}{\Delta_t(1 - \Delta_t)^{3/2}} H_1(t) \right) dt \quad (32)$$

$H_1(t)$ is the same function that was used for calculating $u_\infty(\bar{x}_i, \alpha_i)$ and is reported in the appendix. $K_{Icohe}(t)$ results by interpolating linearly between the values of K_{Icohe} calculated with Eq. (29).

5 NUMERICAL VALIDATION

Analytical predictions corresponding to the fracture behaviour of compact-tension specimens determined with the technique proposed in this work were compared with the *FEM* results found using a commercial code, *ABAQUS/Standard* (ABAQUS, 2005).

The general outline of the specimen analysed is as shown in Fig. 4, considering $B = 16$ mm and $W = 64$ mm. Three different conditions corresponding to initial crack lengths of 35%, 50%, and 65% have been analysed. It is assumed that the material, whose mechanical properties are listed in Table 3, behaves as linear softening.

E (MPa)	ν	σ_c (MPa)	G_F (N/mm)
30000	0,28	3,00	0,10

Table 3: Mechanical properties of the material considered.

Only half the specimen has been simulated using four-node plane-strain elements. Displacements in y -direction to nodes located in the uncracked ligament were restricted. In correspondence with the load direction a displacement, v , was imposed, see Fig. 6.

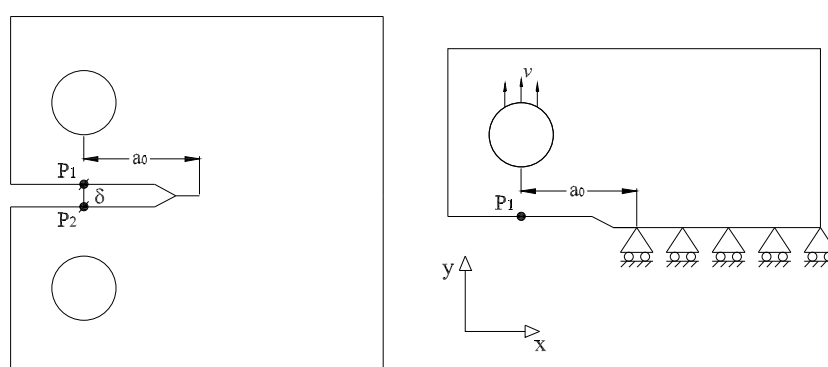


Figure 6: Boundary conditions

Cohesive elements available in the *FEM* code with initial zero thickness were used to model the uncracked ligament. An example of the finite-element meshes used is shown in Fig. 7. For each of the three conditions of analysis, the results found using the *FEM* and the method proposed are shown below.

The solution algorithm was implemented in *MATLAB*, and the governing equations were integrated numerically using Simpson's three-eighths rule (Hildebrand, 1965).

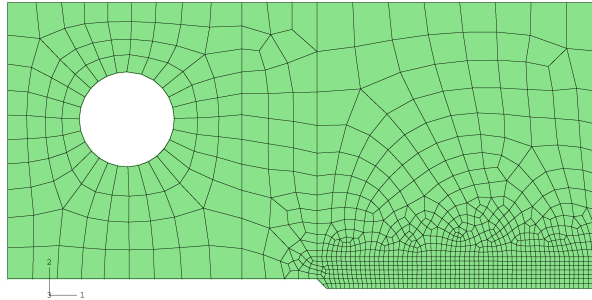


Figure 7: Finite-element mesh used in the simulations

Fig. 8 to 10 represent the variation of the applied load in terms of the $\Delta\delta$, defined as the increment of the distance between two points, P_1 y P_2 , located at the intersection of the lips of the crack to the load direction, as can be seen in Fig. 6. Two curves are shown on any graph corresponding to the proposed method and to the *FEM* results.

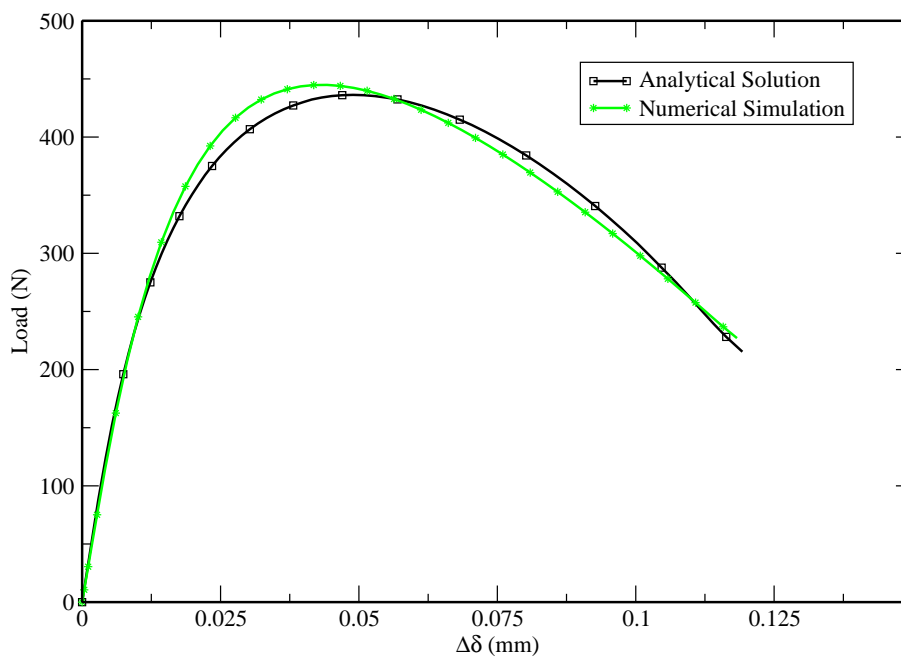
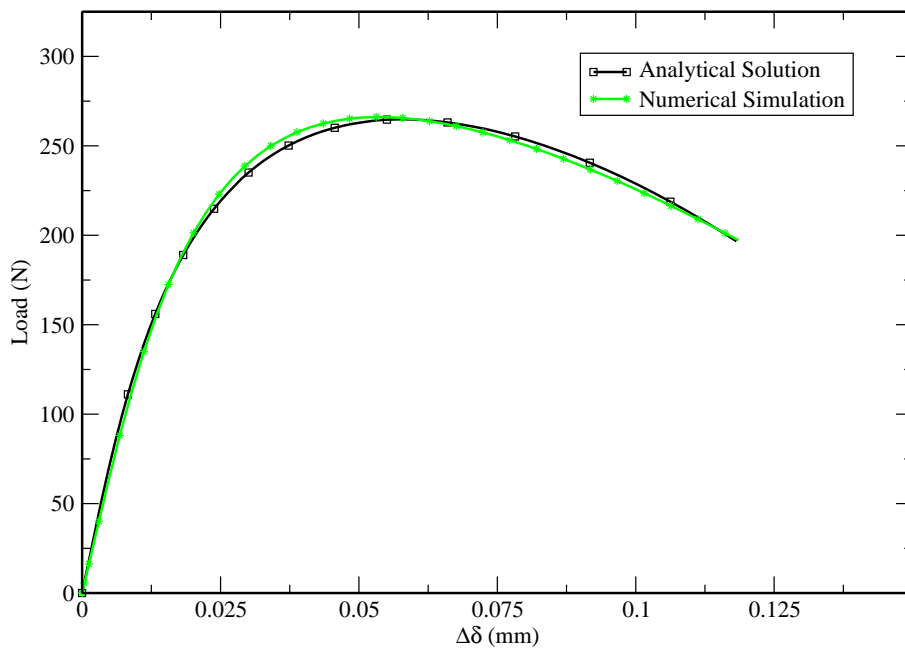
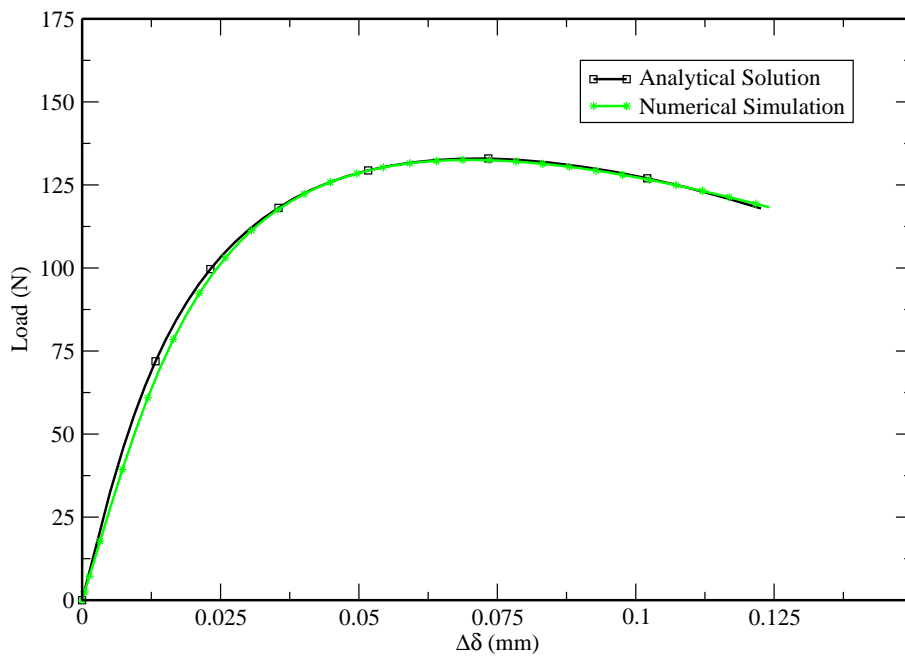


Figure 8: Validation results corresponding to $\alpha = 0,35$

As can be seen, there is a good prediction of the shape of the *load* – $\Delta\delta$ curve, especially in the initial slope. The method is especially powerful to predict the value of both the peak load recorded, as well as the respective $\Delta\delta$. The major differences compared with the *FEM* results remained below 1.5% for the shortest initial crack length.

It should be noted that the results found with the proposed method, in addition to differing very little, are conservative in relation to the *FEM* analysis.

Figure 9: Validation results corresponding to $\alpha = 0,50$ Figure 10: Validation results corresponding to $\alpha = 0,65$

6 EXPERIMENTAL VALIDATION

The analytical method proposed has also been validated by comparing their predictions with experimental results reported in the literature (Gómez et al., 2005). The general outline of the specimen is depicted in Fig. 4, with $B = 16 \text{ mm}$, $W = 64 \text{ mm}$ and $a = 31.50 \text{ mm}$.

The chosen material was a glassy polymer (*PMMA*) whose mechanical properties and softening function are shown in Table 4.

E (MPa)	ν	σ_c (MPa)	G_F (N/mm)	Softening
5050	0,40	128,00	0,48	Rectangular

Table 4: Material properties considered in the experimental validation.

The only reported case has been considered. In Fig. 11 experimental results are shown with the prediction of the analytical method proposed for the same geometry.

As it can be seen, there is an excellent agreement between the shape of the *load* – *CMOD* curve found experimentally and that determined with the proposed method.

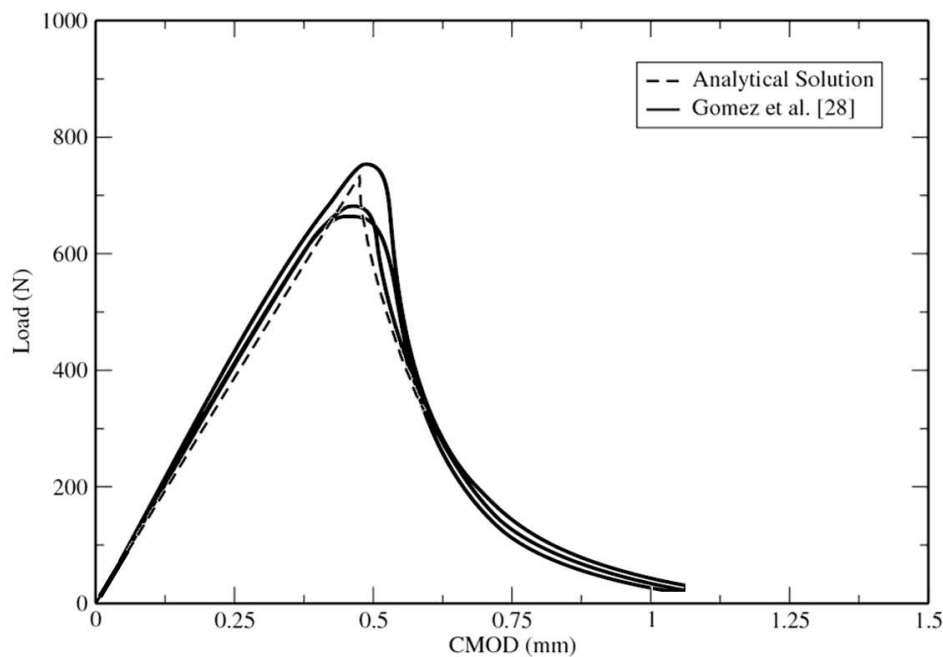


Figure 11: Results of the experimental validation

7 CONCLUSIONS

In this work an analytical investigation on the fracture behaviour of compact-tension test specimens, a configuration extensively used in testing mechanics, has been carried out within the framework of a novel application of the well-known weight-function technique. In addition to the material properties and the weight function, only a general expression of the stress intensity factor is needed.

An algorithm for numerically solving the governing equations has been implemented in *MATLAB*. A linear softening curve is adopted and the predictions of the proposed method have been compared with the numerical results obtained using the finite-element method. The validation involves the analysis of compact-tension specimens with different initial crack lengths and the results demonstrate the benefits of the technique developed here, which yields results without any appreciable error.

The predictions using the methodology proposed by the authors have also been compared with experimental results available in the literature considering a rectangular softening curve. As in the numerical validation, there is an excellent agreement between the shape of the *load – CMOD* curve found experimentally and that determined with the proposed method.

This procedure, which offers an alternative for determining the fracture behaviour of quasi-brittle materials, also has important advantages such as a better ability to modify the geometry as well as the size of the specimen. It allows the fracture behaviour of materials with different characteristic lengths to be analysed, leading to an important saving of time and computing cost with respect to the finite-element method.

REFERENCES

- ABAQUS. *User's Manual Version 6.5*. Karlsson and Sorensen Inc., 2005.
- Barenblatt G. The mathematical theory of equilibrium cracks in brittle fracture. *Advances in Applied Mechanics*, 7:55–129, 1962.
- Bažant Z. Smearred-tip superposition method for nonlinear and time-dependent fracture. *Mechanics Research Communications*, 17:343–351, 1990.
- Bažant Z. and Beissel S. Smearred-tip superposition method for cohesive fracture with rate effect and creep. *International Journal of Fracture*, 65:277–290, 1994.
- Bažant Z. and Planas J. *Fracture and size effect in concrete and other quasibrittle structures*. CRC Press LLC, Boca Raton, EE.UU., 1998.
- Bueckner H. A novel principle for the computation of stress intensity factors. *Zeitschrift für Angewandte Mathematik und Mechanik*, 50:529–546, 1970.
- Dugdale R. Yielding of steel sheets containing slits. *Journal of the Mechanics and Physics of Solids*, 8:100–104, 1960.
- Fett T. and Munz D. *Stress intensity factors and weight functions*. Computational Mechanics Publications, Southampton, U.K., 1997.
- Foot R., Mai Y.W., and Cotterell B. Crack growth resistance curves in strain softening materials. *Journal of the Mechanics and Physics of Solids*, 34:593–607, 1986.
- Gómez F., Elices M., and Planas J. The cohesive crack concept: application to PMMA at -60°C. *Engineering Fracture Mechanics*, 72:1268–1285, 2005.
- Hildebrand F. *Métodos de cálculo para ingenieros*. Aguilar, Madrid, Spain, 1965.
- Hillerborg A. The theoretical basis of a method to determine the fracture energy G_F of concrete. *Materials and Structures*, 18:291–296, 1985.
- Hillerborg A., Modéer M., and Petersson P. Analysis of crack formation and crack growth in concrete by means of fracture mechanics and finite elements. *Cement and Concrete Research*, 6:773–782, 1976.
- Knauss W. The mechanics of polymer fracture. *Applied Mechanics Reviews*, 26:1–17, 1973.
- Knauss W. Time dependent fracture and cohesive zones. *ASME Journal of Engineering Materials and Technology*, 115:262–267, 1993.
- Mai Y.W. and Lawn B. Crack-interface bridging as a fracture resistance mechanism in ceramics: II, theoretical fracture mechanics model. *Journal of the American Ceramic Society*, 70:289–294, 1987.
- Petersson P. Crack growth and development of fracture zone in plain concrete and similar materials. Report Nž TVBM-1006, Division of Building Materials, Lund Institute of Technology, Lund, Sweden, 1981.
- Planas J. and Elices M. Un nuevo método de análisis del comportamiento asintótico de la propagación de una fisura en modo I. *Anales de Mecánica de la Fractura*, 3:219–227, 1986.
- Planas J. and Elices M. Asymptotic analysis of a cohesive crack. 1: Theoretical background. *International Journal of Fracture*, 55:153–177, 1992.
- Reinhardt H. Fracture mechanics of fictitious crack propagation in concrete. *Heron*, 29:3–42, 1984.
- Rice J. Some remarks on elastic crack-tip stress fields. *International Journal of Solids and Structures*, 8:751–758, 1972.
- Srawley J. and Gross B. Stress intensity factors for bend and compact specimens. *Engineering Fracture Mechanics*, 4:587–589, 1972.
- Tijssens M., van der Giessen E., and Sluys L. Modeling of crazing using a cohesive surface

- methodology. *Mechanics of Materials*, 32:19–35, 2000.
- Tvergaard V. and Hutchinson J. The relation between crack growth resistance and fracture process parameters in elastic-plastic solids. *Journal of the Mechanics and Physics of Solids*, 40:1377–1397, 1992.
- Ungsuwarungsri T. and Knauss W. A nonlinear analysis of an equilibrium craze: Part I - Problem formulation and solution. *ASME Journal of Applied Mechanics*, 55:44–51, 1988a.
- Ungsuwarungsri T. and Knauss W. A nonlinear analysis of an equilibrium craze: Part II - Simulations of craze and crack growth. *ASME Journal of Applied Mechanics*, 55:52–58, 1988b.
- Williams J. *Fracture mechanics of polymers*. Ellis Horwood, Ltd., West Sussex, U.K., 1984.
- Yuan H., Lin G., and Cornec A. Verification of a cohesive zone model for ductile fracture. *ASME Journal of Engineering Materials and Technology*, 118:192–200, 1996.

APPENDIX. AUXILIARY FUNCTIONS

The following are the auxiliary functions $H(\alpha)$, $H_1(t)$ and $H_2(t)$.

$$\begin{aligned}
 H(\alpha) = & \{ A_{11} + A_{21}(1 - \rho_i) + A_{31}(1 - \rho_i)^2 + A_{41}(1 - \rho_i)^3 + \\
 & + A_{12}\alpha + A_{22}\alpha(1 - \rho_i) + A_{32}\alpha(1 - \rho_i)^2 + A_{42}\alpha(1 - \rho_i)^3 + \\
 & + A_{13}\alpha^2 + A_{23}\alpha^2(1 - \rho_i) + A_{33}\alpha^2(1 - \rho_i)^2 + A_{43}\alpha^2(1 - \rho_i)^3 + \\
 & + A_{14}\alpha^3 + A_{24}\alpha^3(1 - \rho_i) + A_{34}\alpha^3(1 - \rho_i)^2 + A_{44}\alpha^3(1 - \rho_i)^3 + \\
 & + A_{15}\alpha^4 + A_{25}\alpha^4(1 - \rho_i) + A_{35}\alpha^4(1 - \rho_i)^2 + A_{45}\alpha^4(1 - \rho_i)^3 \}
 \end{aligned}$$

where

$$\rho_i = \frac{\bar{x}_i}{\alpha}$$

$$\begin{aligned}
 H_1(t) = & \left\{ A_{11} + \frac{t^2}{\bar{x}_i + t^2} \left[A_{21} + A_{31} \frac{t^2}{\bar{x}_i + t^2} + A_{41} \left(\frac{t^2}{\bar{x}_i + t^2} \right)^2 \right] + \right. \\
 & + (\bar{x}_i + t^2) \left[A_{12} + \frac{t^2}{\bar{x}_i + t^2} \left(A_{22} + A_{32} \frac{t^2}{\bar{x}_i + t^2} + A_{42} \left(\frac{t^2}{\bar{x}_i + t^2} \right)^2 \right) \right] + \\
 & + (\bar{x}_i + t^2)^2 \left[A_{13} + \frac{t^2}{\bar{x}_i + t^2} \left(A_{23} + A_{33} \frac{t^2}{\bar{x}_i + t^2} + A_{43} \left(\frac{t^2}{\bar{x}_i + t^2} \right)^2 \right) \right] + \\
 & + (\bar{x}_i + t^2)^3 \left[A_{14} + \frac{t^2}{\bar{x}_i + t^2} \left(A_{24} + A_{34} \frac{t^2}{\bar{x}_i + t^2} + A_{44} \left(\frac{t^2}{\bar{x}_i + t^2} \right)^2 \right) \right] + \\
 & \left. + (\bar{x}_i + t^2)^4 \left[A_{15} + \frac{t^2}{\bar{x}_i + t^2} \left(A_{25} + A_{35} \frac{t^2}{\bar{x}_i + t^2} + A_{45} \left(\frac{t^2}{\bar{x}_i + t^2} \right)^2 \right) \right] \right\}
 \end{aligned}$$

$$\begin{aligned}
 H_2(t) = & \left\{ A_{11} + A_{21} \left(\frac{t^2}{\alpha_i} \right) + A_{31} \left(\frac{t^2}{\alpha_i} \right)^2 + A_{41} \left(\frac{t^2}{\alpha_i} \right)^3 + \right. \\
 & + \alpha_i \left[A_{12} + A_{22} \left(\frac{t^2}{\alpha_i} \right) + A_{32} \left(\frac{t^2}{\alpha_i} \right)^2 + A_{42} \left(\frac{t^2}{\alpha_i} \right)^3 \right] + \\
 & + \alpha_i^2 \left[A_{13} + A_{23} \left(\frac{t^2}{\alpha_i} \right) + A_{33} \left(\frac{t^2}{\alpha_i} \right)^2 + A_{43} \left(\frac{t^2}{\alpha_i} \right)^3 \right] + \\
 & + \alpha_i^3 \left[A_{14} + A_{24} \left(\frac{t^2}{\alpha_i} \right) + A_{34} \left(\frac{t^2}{\alpha_i} \right)^2 + A_{44} \left(\frac{t^2}{\alpha_i} \right)^3 \right] + \\
 & \left. + \alpha_i^4 \left[A_{15} + A_{25} \left(\frac{t^2}{\alpha_i} \right) + A_{35} \left(\frac{t^2}{\alpha_i} \right)^2 + A_{45} \left(\frac{t^2}{\alpha_i} \right)^3 \right] \right\}
 \end{aligned}$$

The values of the coefficients $A_{\eta\mu}$ are shown in Table 2.